Charge-Carrier Dynamics in Organic-Inorganic Metal Halide Perovskites

Laura M. Herz

Department of Physics, University of Oxford, OX1 3PU Oxford, United Kingdom; email: laura.herz@physics.ox.ac.uk

Annu. Rev. Phys. Chem. 2016. 67:65–89

First published online as a Review in Advance on February 26, 2016

The *Annual Review of Physical Chemistry* is online at physchem.annualreviews.org

This article's doi: 10.1146/annurev-physchem-040215-112222

Keywords

photovoltaic, excitons, free charge carriers, charge-carrier recombination, bimolecular, Auger, traps

Abstract

Hybrid organic-inorganic metal halide perovskites have recently emerged as exciting new light-harvesting and charge-transporting materials for efficient photovoltaic devices. Yet knowledge of the nature of the photogenerated excitations and their subsequent dynamics is only just emerging. This article reviews the current state of the field, focusing first on a description of the crystal and electronic band structure that give rise to the strong optical transitions that enable light harvesting. An overview is presented of the numerous experimental approaches toward determining values for exciton binding energies, which appear to be small (a few milli-electron volts to a few tens of milli-electron volts) and depend significantly on temperature because of associated changes in the dielectric function. Experimental evidence for charge-carrier relaxation dynamics within the first few picoseconds after excitation is discussed in terms of thermalization, cooling, and many-body effects. Charge-carrier recombination mechanisms are reviewed, encompassing trap-assisted nonradiative recombination that is highly specific to processing conditions, radiative bimolecular (electron-hole) recombination, and nonradiative many-body (Auger) mechanisms.

1. INTRODUCTION

Photovoltaic cells incorporating hybrid organic-inorganic metal halide perovskites have seen a phenomenally rapid rise in power conversion efficiencies (PCE) over the past 5 years (1). Following initial demonstrations of perovskite-sensitized liquid-electrolyte solar cells (2), the development of all-solid-state device architectures in 2012 triggered a fast rise in PCE toward 10% (3, 4). These initial studies were based on methylammonium lead tri-iodide, which rapidly became the most commonly investigated material. Optimization of processing conditions, material design, and device architecture led to further rapid improvements (5–8), with PCEs of over 20% reported in 2015 (1, 9). **Figure 1*c*** illustrates two of the most commonly implemented device architectures: the dye-sensitized solar cell (DSSC) and the planar heterojunction concept. In the DSSC arrangement, light is absorbed in the perovskite sensitizer acting as the "dye," after which electrons may transfer into the mesoporous TiO_2 and holes into the hole-transporting material (HTM) (4, 10). In the simplified planar heterojunction architecture (6), electron-hole pairs generated in the perovskite absorber must diffuse to the selective HTM and electron-transporting material layers, requiring sufficiently high charge-carrier diffusion lengths. In a third concept, the meso-superstructured configuration, an insulating mesoporous Al_2O_3 scaffold aids coating uniformity (3, 5). Following the initial success of these materials as active ingredients in photovoltaics, a parallel strand of research soon emerged, focusing on light-emitting diodes (11, 12) and amplified spontaneous emission or lasing (13–17). Although applications based on these materials have hence progressed

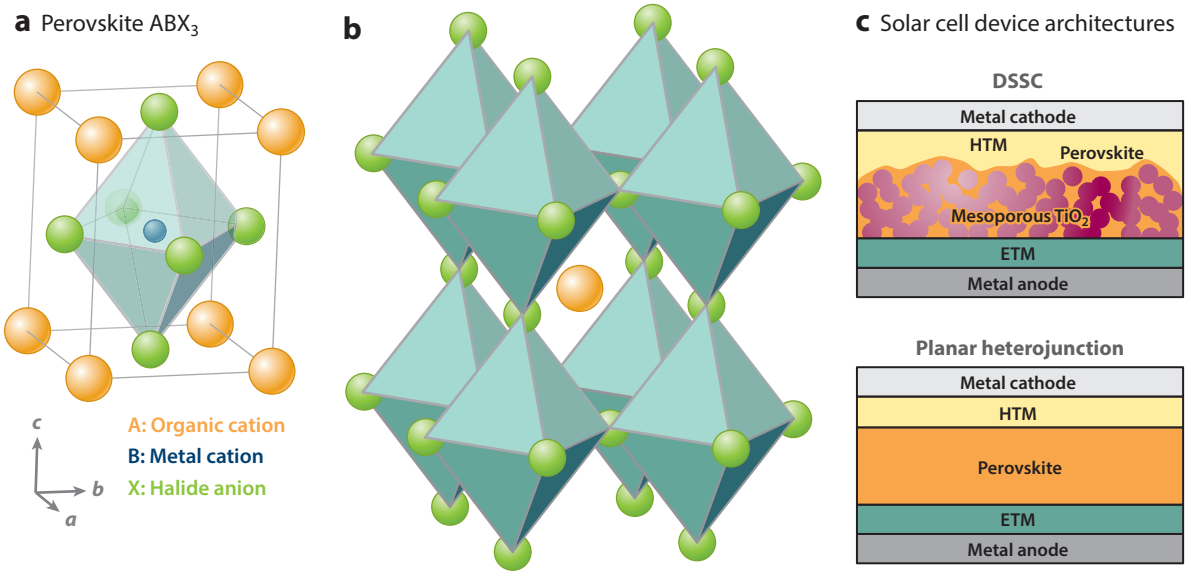

Figure 1

(*a*) Perovskite unit cell of the pseudocubic lattice showing the organic A cation (e.g., methylammonium, formamidinium) in orange, the metal B cation (e.g., Pb^{2+} or Sn^{2+}) in blue, and the X anion (e.g., Cl^-, Br^-, or I^-) in green. (*b*) Representation of the perovskite lattice in terms of an anion corner-shared 3D network of $(BX_6)^{4-}$ octahedra, with B cations at their centers and A cations between them. Octahedral tilt combinations result in the adopted crystal symmetry space group. (*c*) Schematic depiction of two typical device architectures commonly used for perovskite solar cells: the dye-sensitized solar cell (DSSC) arrangement and the simplified planar heterojunction architecture. Typical materials used in high-performing photovoltaics cells are as follows: a nontransparent electrode (silver or gold), a transparent electrode (e.g., fluorine tin oxide), a hole-transporting material (HTM; spiro-OMeTAD or PEDOT:PSS), and an electron-transporting material (ETM; compact TiO_2 or PCBM) (18). A transparent substrate (e.g., glass) is situated below (above) the anode (cathode) in the normal (inverted) configuration to provide support.

at an amazing speed, an understanding of the fundamental photophysics enabling such success is only just emerging. Yet such knowledge is critical for the design of high-performance materials because the generation, relaxation, and recombination of photoexcited charge species have a direct bearing on how effectively light is converted into electrical current, and vice versa. This review summarizes the current state of the field, providing a detailed summary of ongoing research elucidating the fundamental nature of photoexcited states and their dynamics in hybrid metal halide perovskites.

Strictly speaking, perovskite is the calcium titanium oxide mineral $CaTiO_3$ named after the Russian mineralogist Lev Perovski. Compounds of the same crystal structure type are said to assume a perovskite structure (19) as shown in **Figure 1*a*,*b*** with A cations (organic cations) in the corners, the B cation (metal cation) at the center, and the X anion (halide anion) centered on the faces of the unit cell. Goldschmidt (19) proposed in 1926 that a solid will only assume the perovskite structure if the respective ionic radii R_A, R_B, and R_X fulfill the relation $R_A + R_X = t \times \sqrt{2}(R_B + R_X)$, with the tolerance factor t ranging between 0.8 and 1. A large number of materials exist within the perovskite structure (20, 21); however, highly efficient photovoltaic cells using such perovskite materials as light absorbers have so far been demonstrated only for X anions composing halogens such as I^-, Br^-, and Cl^-. Within the stoichiometry ABX_3, the halogen anion needs to be counterbalanced by a monovalent and a divalent A and B species for overall charge neutrality. In fully inorganic metal halide perovskites, the monovalent metal may, for example, be an alkali such as Cs^+ and the divalent species Pb^{2+}, Sn^{2+}, or Ge^{2+}. In hybrid organic-inorganic halide perovskites, which are the highest-performing active materials in photovoltaic cells to date, the monovalent metal is replaced by an organic cation of single positive charge. The most commonly used organic A ion is methylammonium (MA), $CH_3NH_3^+$ (3), but formamidinium (FA), $H_2NCHNH_2^+$ (22), and mixed systems (9) are also emerging with excellent results. The divalent metal (B cation) utilized in the best performing active materials for such perovskite photovoltaics has almost exclusively been lead (Pb^{2+}), which has the additional benefit of being an abundant material in Earth's ore (23). However, concerns about lead's toxicity have triggered a search for alternative B cations. The tin-based perovskite $MASnI_3$ has been demonstrated to allow for photovoltaic PCEs of approximately 6% (24, 25), which is respectable but still lower than those reported for their lead-containing counterparts [now exceeding 20% (1)].

This review predominantly focuses on hybrid organic-inorganic halide perovskite materials that have shown particular promise for photovoltaic applications, that is, materials for which A is either the MA or FA cation, B is Pb^{2+} unless stated otherwise, and X is the halogen anion I^-, Br^-, or Cl^- or a mixture thereof. The mixed halide perovskite material $MAPbBr_yI_{3-y}$ ($0 \leq y \leq 3$) exhibits a band gap that tunes continuously between ~1.5 eV and ~2.2 eV with an increasing bromide fraction $y/3$ (26), making this system attractive for tandem cells, for example. However, the apparent chloride equivalent $MAPbCl_xI_{3-x}$ showed no evidence for band-gap shifts when chlorine was included in the solution precursor materials (3). It should be stressed that this material is generally produced from the organic and inorganic precursors MAI and $PbCl_2$ mixed in the ratio 3:1; therefore, no inclusion of chloride is in principle required for the formation of the perovskite structure, given that excess components can leave the materials upon annealing (3). Subsequent experimental examination (27–29) of the composition of $MAPbCl_xI_{3-x}$ revealed that the fraction of chloride contained is indeed very small (in the percent region). Density-functional calculations suggest that this results from a lower formation energy (by ~160 meV) of $MAPbI_3$ ($x = 0$) with respect to a mixed ($x = 1$) system (30). Therefore, $MAPbCl_xI_{3-x}$ ought to display similar photophysics to $MAPbI_3$. That said, the materials have been shown to vary in their morphology and grain boundary states (31), which may cause the observed differences in recombination dynamics (32) and charge-carrier diffusion lengths (33). In the following, particular emphasis is

given to $MAPbI_3$, which can be seen as a prototypical material for perovskite photovoltaics and has been most carefully examined in terms of its optoelectronic properties.

2. NATURE OF PHOTOEXCITED STATES

Any meaningful analysis of the dynamics of photoexcited states in hybrid metal halide perovskites requires careful examination of the nature of such states. This section summarizes the current knowledge on the crystal structure and associated electronic band structure for hybrid metal halide perovskites and presents an overview of the current debate on the significance of excitonic effects.

2.1. Electronic Structure

In this section, we provide an overview of the lattice (crystal structure) properties of hybrid lead halide perovskites and discuss the resulting electronic band structure.

2.1.1. Crystal structure and phase transitions. Materials adopting the perovskite structure have a natural propensity toward undergoing structural phase transitions. As shown in **Figure 1**, the perovskite crystal can be viewed as an anion corner-shared 3D network of $(BX_6)^{4-}$ octahedra, with B cations at their centers and A cations between them. In 1972, Glazer (21) showed that the tilting of such octahedra has a direct bearing on the pseudocubic lattice parameters and devised a system linking octahedral tilt combinations to symmetry space groups. The resulting crystal structure of the perovskite type commonly adopts, for example, cubic, tetragonal, trigonal, or orthorhombic phases in a wide range of perovskite materials (21). Similarly, many hybrid metal halide solids exhibit structural phase transitions at multiple temperature points (34–39). These transitions need to be considered when assessing charge-carrier dynamics because they may alter the electronic band structure and therefore optoelectronic properties of the material (34, 40). The commonly studied $MAPbI_3$, for example, adopts a simple cubic perovskite structure (space group $Pm\bar{3}m$; 36, 37, 39) at temperatures above ~315–330 K, although a very small ferroelectric-type displacement of the lead cation has been observed (34), which may establish a tetragonal unit cell (space group *P4mm*). The transition to the room-temperature phase involves a collective rotation of the PbI_6 octahedra around the *c* axis (36, 37), which is known to occur for many inorganic perovskites and leads to tetragonal space group *I4/mcm* with closer packing within the *ab* plane (36, 37). A further transition to an orthorhombic phase (space group *Pnma*) is observed at ~160 K (36, 38), which is accompanied by a tilting of the PbI_6 octahedra out of the *ab* plane (38). Baikie et al. (38) suggested that, by symmetry, a continuous transition between the tetragonal and orthorhombic phases is not possible and postulated the existence of a transient intermediate phase. For simplicity, the cubic phase adopted by $MAPbI_3$ above ~330 K is referred to as the high-temperature (HT) phase, the tetragonal phase between ~330 and 160 K as the room-temperature (RT) phase, and the orthorhombic phase between ~160 and 0 K as the low-temperature (LT) phase.

An important difference between the hybrid perovskite $MAPbI_3$ and purely inorganic perovskites is the presence of the polar A cation $CH_3NH_3^+$, which has several rotational degrees of freedom in both RT and HT phases. These have been investigated by NMR spectroscopy (39), infrared (IR) vibrational spectroscopy (41), calorimetry (42), and dielectric measurements (36, 41). Two-dimensional infrared vibrational anisotropy spectroscopy has recently revealed the timescales for $CH_3NH_3^+$ rotation in $MAPbI_3$ at room temperature, revealing a fast (300-fs) wobbling-in-a-cone motion and a slow (3-ps) jump-like reorientation (43). Whereas both the RT and HT phases exhibit complete orientational disorder of $CH_3NH_3^+$, the transition from the RT tetragonal to the LT orthorhombic phase results in severe reduction of such disorder (39, 42). As a result, the

HT → RT phase transition at ~330 K induces a smaller change in the optoelectronic properties of $MAPbI_3$ than the RT → LT transition at ~160 K (44). Significant changes in exciton binding energy are also observed at ~160 K, as discussed in detail below.

2.1.2. Band structure and optical transitions. The electronic structure of organic lead halide perovskites has been repeatedly examined with density-functional theory (DFT) calculations by several research groups (30, 38, 40, 45, 47–51). As an example, **Figure 2*a*** shows a schematic representation of the calculated band structure for $MAPbI_3$ at room temperature near the high-symmetry point *R*, which is associated with the band-edge absorption. The valence band maximum (VBM) at *R* is formed of antibonding states derived from hybridizations of the atomic 5p orbitals of iodine and 6s orbitals of lead, whereas the conduction band minimum (CBM) is mainly formed of empty 6p orbitals of lead (30, 47–49). The heavy nature of the lead and iodine ions leads to significant spin-orbit coupling, lowering the band gap and causing a splitting of the conduction band states with the lower, split-off band forming the CBM (40, 47, 48). Optically allowed transitions of electrons from the VBM to the CBM at *R* correspond to the band-gap energy E_g, as observable in the strong absorption onset at ~1.6 eV (see **Figure 2*b***). A clear connection in reciprocal space exists between the *M* and *R* points (30, 38, 45), allowing the photogeneration of electron-hole pairs across a wide range of visible wavelengths (45), which can subsequently relax into the *R* valley (see also Section 3). These transitions lead to the observed absorption continuum for photon energies above E_g (e.g., in the transmission spectra of thin $MAPbI_3$ films) (**Figure 2*b***). In addition, higher-energy absorption features may arise from transitions involving higher (lower)-lying states of the correct symmetry (45) at the *R* point (see vertical arrows in **Figure 2*a***).

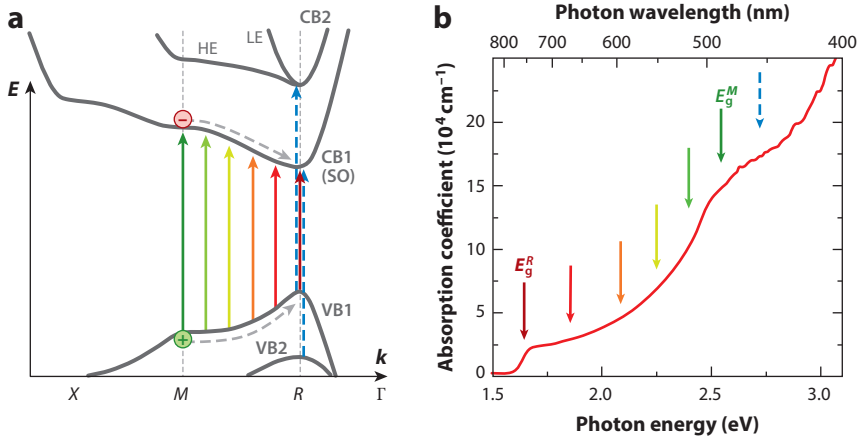

Figure 2

(*a*) Electronic band structure of $MAPbI_3$, adopted from density-functional theory calculations presented in References 40 and 45. Colored upward-pointing arrows represent allowed photoinduced electronic transitions. The lowest CB (CB1) is the spin-orbit SO band, whereas the higher-lying CB2 comprises HE and LE states, according to References 40 and 45. The dashed blue arrows indicate the partly dipole-allowed transitions VB2 → CB1 and VB1 → CB2 at the *R* point. (*b*) Absorption spectrum showing that a continuum of electronic transitions between the *R* and *M* valleys leads to strong absorption across the visible range (46). Relaxation toward the *R* valley gives rise to a photoluminescence peak near 1.6 eV arising from CBM1 → VBM1 transitions at the *R* point. Abbreviations: CB, conduction band; CBM, conduction band minimum; HE, heavy electron; LE, light electron; SO, split-off; VB, valence band; VBM, valence band maximum.

Changes in band structure with compositional modification have also been examined in detail for hybrid lead halide systems. First-principles calculations suggested that substitution of the halide X in $MAPbX_3$ along the line of increasing atomic size (Cl → Br → I) will lead to a decrease in the band gap (30, 47), in agreement with experimental trends observed for the absorption onset in $MAPbBr_yI_{3-y}$ and $FAPbBr_yI_{3-y}$ (22, 47). Similarly, substitution of the organic halide was experimentally found to shift the absorption onset energy downward in the order of increasing cation size, that is, from ∼1.6 eV to ∼1.5 eV when the MA cation in $MAPbI_3$ was replaced with larger-radius FA^+, or up to ∼1.7 eV when MA^+ was replaced with the smaller Cs^+(22, 34). However, opposite effects are observed when the larger lead cation is replaced with the smaller tin cation: The absorption onset shifts downward from ∼1.6 eV for $MAPbI_3$ to ∼1.2 eV for $MASnI_3$ (24, 25, 34). Comparison of such trends highlights the absence of a clear-cut correlation between changes in ionic size (and therefore a presumed pseudocubic lattice constant) and trends in band-gap energy. The reasons here appear to derive from the complex interplay between other factors affecting the band-gap energy (52, 53), such as sizeable spin-orbit coupling and tilting of the octahedra illustrated in **Figure 1**. DFT calculations by Amat et al. (52) suggested that the decrease in band gap along the organic cation substitution MA → FA in $MAPbI_3$ is caused by the comparatively higher propensity of FA to form hydrogen bonds with the inorganic matrix, leading to pseudocubic structures with decreased octahedral tilting. This in turn alters the ionic character of the Pb–I bond, which enhances the lead character of the conduction band states and therefore spin-orbit coupling, lowering the band gap for $FAPbI_3$. Even and colleagues (53) similarly reported a significant interplay between structural distortions and spin-orbit coupling for the $MABCl_3$ (B = Pb, Sn, Ge) system. These examples emphasize the complexity of theoretical modeling required to accurately reflect experimental findings in these systems.

2.2. Excitons Versus Free Charge Carriers

Many initial investigations of the photogenerated species in $MAPbI_3$ have aimed to resolve the question of whether excitations feature strong excitonic character or are better described as free charge-carrier densities (45, 47, 54–64). Coulomb correlations between electrons and holes affect the operation of photovoltaic cells because the resulting bound state (exciton) has an associated binding energy E_b that needs to be overcome for electrons and holes to contribute to the photocurrent. However, for $E_b > kT$, thermal energies may suffice to dissociate the exciton; therefore, exciton binding energies below thermal energies at room temperature (26 meV) are highly desirable.

Unfortunately, this target is unreachable for many solution-processed materials used as light-harvesting materials for photovoltaics (65), such as π-conjugated molecular solids employed in organic photovoltaics (OPV) (66, 67) and sensitizers used in DSSCs (68). Exciton binding energies postulated for organic molecular semiconductors such as π-conjugated polymers are typically in the range of several hundred milli-electron volts (69, 70) as a result of the generally low value of the dielectric function. Excitations in organic solids are therefore best described as Frenkel excitons that are spatially localized and show significant polaronic character because of coupling between electronic transitions to the lattice (nuclear bonds) (71). In typical OPV or DSSC applications, therefore, additional effort is needed to ensure dissociation of excitons at room temperature, typically through the use of complex nanostructured materials with their associated morphological complexities and instabilities.

In contrast, incipient time-resolved spectroscopic experiments on solution-processed thin films of $MAPbI_3$ surprisingly suggested that the primary species generated after photoexcitation were free charges (32, 33, 72, 73). Similar dynamics were observed after pulsed photoexcitation of

$MAPbI_{3-x}Cl_x$ films when probed by photoluminescence and transient absorption spectroscopy near the band edge, suggesting the presence of only one photogenerated species (33). In addition, photoinduced terahertz conductivity dynamics of $MAPbI_3$ and $MAPbI_{3-x}Cl_x$ (32) showed that only one type of species appeared to contribute, which was identified as free charge carriers from the Drude-like conductivity spectrum and strong bimolecular recombination component (see also Section 4.2). Subsequently, both photoluminescence and band-edge absorption dynamics in $MAPbI_3$ films were found to be governed by the same bimolecular recombination rate constant, suggesting that the emission at room temperature originates predominantly from a free-charge-carrier density (72). Correlation between the photoinduced terahertz conductivity and the band-edge absorption dynamics of $MAPbI_3$ again suggested the presence of only one species at room temperature (73). Therefore, excitonic effects appeared to be relatively insignificant at room temperature, much to the delight of the photovoltaic research community.

These studies suggest, in accordance with earlier findings on polycrystalline $MAPbI_3$ (47, 54), that the exciton binding energy for $MAPbI_3$ is sufficiently low for excitons to be described within the Wannier-Mott model. Wannier excitons are a hydrogen-like species comprising a conduction band electron of effective mass m_e^* and a valence band hole of effective mass m_h^* moving in a dielectric medium with relative permittivity (or dielectric function) ϵ as bound states with energies

$$E_n = -\frac{m_r^* e^4}{8h^2\epsilon_0^2\epsilon^2}\frac{1}{n^2} = -\frac{E_b}{n^2} \quad (1)$$

below the relevant band edge, where $m_r^* = ((m_e^*)^{-1} + (m_h^*)^{-1})^{-1}$ is the reduced mass of the electron-hole system. Excited states in $MAPbI_3$ are therefore much closer in nature to those found in typical inorganic semiconductors such as GaAs than those present in organic molecular solids. It is interesting to note that across a wide data set of direct-gap inorganic semiconductors, an empirical correlation between band gap E_g and exciton binding energy E_b has long been established (74, pp. 165–66), which derives from a general trend of effective masses and ϵ with E_g. From such data, and the band-gap energy of $MAPbI_3$ (~1.6 eV), one would estimate the exciton binding energy to fall in the range 2–20 meV. However, as this spread indicates, there are strong variations of the exciton binding energies even for semiconductors with identical band gaps, which may, for example, arise from real-space localization or ionic effects (75). Therefore, an accurate determination of the exciton binding energy in $MAPbI_3$ would be highly desirable. However, to date, an astonishingly wide range of experimentally determined values of E_b has been reported for $MAPbI_3$ (45, 47, 54–64), from 2 meV to 62 meV (see **Table 1**). As discussed below, there are inherent difficulties in the determination of E_b for this material system. First, the temperature range that can be probed for any particular crystal structure is limited owing to phase transitions, and any reported exciton binding energy may be specific to the phase explored (45, 56, 61). Second, strong changes occur in the value of the dielectric function with frequency and temperature (36, 41). Third, material variability and morphology may still have some influence over the observed optical properties near the band edge (57, 76).

2.2.1. E_b from diamagnetic shifts of magnetoabsorption. First reported studies of exciton binding energies for $MAPbI_3$ were based on magnetoabsorption spectroscopy at low temperatures (4.2 K), which followed the diamagnetic shift of the prominent absorption feature with the applied magnetic field to derive the diamagnetic coefficient c_0 (47, 54). To extract an exciton binding energy from c_0, Hirasawa et al. (54) used the high-frequency (optical) value of the dielectric function ϵ (assumed to be 6.5) to obtain a value of 37 meV for the LT (orthorhombic) phase of $MAPbI_3$; a later, analogous study by Tanaka et al. (47) yielded a value of 50 meV. However, as pointed out in several later articles (45, 55, 56), the choice of ϵ used to evaluate the exciton

Table 1 Exciton binding energies E_b reported for $MAPbI_3$ and $MAPbI_{3-x}Cl_x$

E_b (meV)	Temperature range[a] (K)	Phase[b]	Experimental approach	Reference
5	215–300	RT	Fit of Elliott's theory to band edge	45
9	300	RT	Fit of Elliott's theory to band edge	63
15 → 6	160 → 300	RT	Fit of Elliott's theory to band edge	61
19	10–300	RT/LT[d]	Thermally activated photoluminescence quenching	58
25	170 & 300	RT	Fit of Elliott's theory to band edge	62
29	170–300	RT	Spectrally integrated normalized absorption near band edge	64
32	80–300	RT/LT[d]	Thermally activated photoluminescence quenching	59
55	160–300	RT	Thermal broadening of absorption onset	57
62	160–300	RT	Thermally activated photoluminescence quenching	60
2	4.2	LT[c]	Reassessment of References 47 and 54 using ϵ ($\nu = 20$ Hz, $T = 300$ K)	55
15	50–160	LT	Fit of Elliott's theory to band edge	45
16	2	LT	1s and 2p excitonic magnetoabsorption	56
30 → 20	13 → 150	LT	Fit of Elliott's theory to band edge	61
34	80–140	LT	Spectrally integrated normalized absorption near band edge	64
37	4.2	LT	Diamagnetic shifts in magnetoabsorption using ϵ (ν_{opt})	54
50	4.2	LT	Diamagnetic shifts in magnetoabsorption using ϵ (ν_{opt})	47

[a]Dashes indicate a range over which constant E_b was either assumed or found constant, whereas right arrows highlight trends in E_b with temperature.
[b]RT represents the room-temperature tetragonal phase present in the temperature range 160–330 K, whereas LT represents the low-temperature orthorhombic phase present between 0 and 160 K (see Section 2.1.1).
[c]Assessment combined a low-temperature (4.2 K) diamagnetic coefficient determined in References 47 and 54 with a room-temperature, low-frequency (20 Hz) value of the dielectric function measured in Reference 55.
[d]A broad temperature range across the phase transition at 160 K was analyzed, including data within both LT and RT phases, which were analyzed to yield the value for E_b.

binding energy is not as straightforward as it may seem. In particular, the dielectric function for $MAPbI_3$ shows large variation with both frequency (55, 77) and temperature (36, 41), which leads to a large dependence of the calculated exciton binding energy on the choice of ϵ. Lin et al. (55) re-evaluated the low-temperature data by Hirasawa et al. and Tanaka et al. using the near-static limit of the dielectric function (taken to be 70 measured at a frequency of 20 Hz using room-temperature impedance spectroscopy) and obtained a modified value of $E_b \sim 2$ meV. However, even the alternative use of the static value ϵ_s is not entirely satisfactory as the correct choice of ϵ depends on the relationship between the energy $\hbar\omega_{LO}$ of optical phonons and the exciton binding energy E_b. Static values may only be used if the exciton binding energy is clearly smaller than $\hbar\omega_{LO}$ (i.e., the excitonic Bohr radius is larger than the radius of a polaron) (74, pp. 165–66). For the reverse case of $E_b \geq \hbar\omega_{LO}$, a value between ϵ_s and those encountered at higher frequencies should be taken, given that the polarization of the lattice then cannot fully follow the motion of the electron-hole pair (74, pp. 165–66). It is still unclear which of the two scenarios apply to $MAPbI_3$ as a number of vibrational modes have recently been identified in the energy range into which the exciton binding energy may realistically fall. Terahertz transmission spectroscopy of $MAPbI_{3-x}Cl_x$ has identified two IR-active modes (78), at 1 THz (4 meV) and 2 THz (8 meV), while studies combining either Raman (79) or infrared (80) spectroscopy with DFT calculations for $MAPbI_3$ have assigned low-energy modes in the range 1.9 THz (8 meV) to bending and stretching of the lead-halide bonds. Therefore, a determination of the exciton binding energy

from methods relying on the assumption of a particular value of the dielectric function is best avoided because an accurate choice of ϵ in essence relies on prior knowledge of E_b, or at least requires a self-consistent, iterative approach.

2.2.2. E_b from temperature dependence of the photoluminescence intensity. Alternatively, investigations have drawn on the temperature dependence of the emitted luminescence to arrive at an estimate of the exciton binding energy (58–60). Such experiments were conducted both within the RT phase of $MAPbI_3$ (60) and across the RT and LT phases (58, 59) for which, interestingly, no sudden change in luminescence efficiency at the phase transition temperature (~160 K) was discernable. All studies reported a decrease in emitted photoluminescence intensity with increasing temperature, which was attributed to temperature-activated exciton dissociation. These investigations used the same Boltzmann activation approach to fit data and extracted an exciton binding constant, yet the outcome markedly differed, yielding $E_b = 19$ meV (58) and 32 meV (59) for $MAPbI_3$, and 62 meV (60) for $MAPbI_{3-x}Cl_x$. The observed spread in the application of the same method is surprising, in particular given that $MAPbI_{3-x}Cl_x$ has been shown to contain very little chlorine (27–29) and hence ought to exhibit similar E_b. In addition, it is unclear why exciton dissociation should generally necessitate fluorescence quenching—a number of studies have highlighted that efficient fluorescence originates from free charge carriers at room temperature (11, 81, 82). As discussed in detail in Section 4, the various free-charge recombination mechanisms present in hybrid perovskites are associated with very different radiative efficiencies and temperature dependences (44). As a result, complex dependences of the radiative emission yield on temperature can be expected even if excitonic effects are fully absent, making it difficult to extrapolate E_b from such methods.

2.2.3. E_b from analysis of absorption onsets. An alternative approach toward determining a value for the exciton binding energy has been associated with analysis of the absorption spectra near the band edge. D'Innocenzo et al. (57) extracted the width of the band-edge absorption features as a function of temperature in the range 150–290 K, suggesting an exciton binding energy of (55 ± 20) meV from fits to data assuming a coexistence of homogeneous excitonic broadening mechanisms and temperature-independent inhomogeneous broadening arising from disorder. Other studies (45, 61–63) have taken a different approach, analyzing the full shape of the absorption onset using Elliott's (83) theory of band-onset absorption in a direct semiconductor subject to excitonic effects. This method has the added advantage of yielding a value for the exciton binding energy at any given temperature, thus allowing the influence on E_b of phase changes or temperature variations in ϵ to be explored. In the absence of excitonic effects, the absorption coefficient α for photons with energy E incident on a material is given by $\alpha \propto \sqrt{E - E_g}$ near the absorption onset where bands can be approximated to be parabolic. The presence of Coulombic interactions will lead to additional absorption features below the absorption onset at the energies given by Equation 1, but will also enhance the absorption in the continuum states (83; 84, pp. 275–76). Interestingly, while several separate studies report temperature-dependent exciton binding energies using this method, considerable variations in values emerge again. Even and colleagues (45) reported a relatively constant E_b of 5 meV for the HT (160–330 K) tetragonal phase of $MAPbI_3$, which increases relatively abruptly to 15 meV in the LT (0–160 K) orthorhombic phase. Yamada et al. (61) analyzed a large number of absorption spectra in the temperature range 13–300 K and observed a more gradual increase in exciton binding energy from approximately 6–10 meV near 300 K to 30 meV at 13 K. Saba et al. (62) modeled absorption onsets for 300 K and 170 K and extracted $E_b = 25$ meV. Yang et al. (63) used the method to extract $E_b \sim 9$ meV at room temperature. Thus, exciton binding energies extracted through this method vary between

15 and 30 meV for the LT orthorhombic phase and 5 and 25 meV for the RT phase, with widely different values reported even for spectral absorption features that appear very similar. One possibility for the large variation may lie in the necessary incorporation of lineshape broadening mechanisms, which may add to fitting uncertainties (64) because the excitonic resonances are not clearly separated from the continuum onset for $MAPbI_3$. Sestu et al. (64) therefore recently used an alternative method based on fits to the temperature-dependence of the integrated absorption near the onset, normalized to a value at a particular energy. This method should be less sensitive to lineshape broadening, which does not affect the overall oscillator strength but rather distributes it spectrally. Sestu et al. reported an exciton binding energy of 29 meV at room temperature, which remained constant as the temperature was lowered to the tetragonal to orthorhombic phase transition, below which it increased moderately to 34 meV. Therefore, several studies (45, 61, 64) agree that the exciton binding energy of $MAPbI_3$ is a function of temperature.

2.2.4. E_b from excitonic resonances in magnetoabsorption. A recent study by Miyata et al. (56) suggested an exciton binding energy of 16 meV at low temperature. Here again, these authors investigated magnetoabsorption at high magnetic fields; however, unlike in previous studies (47, 54), Miyata et al. were able to observe both 1s and 2s excitonic absorption features, which allowed for a direct evaluation of the exciton binding energy without recourse to assumptions on the value of ϵ. Unfortunately, an analogous analysis of the magnetoabsorption spectra above the phase transition into the RT phase was hampered by thermal broadening. However, the authors estimated that the binding energy collapses to a few milli-electron volts in this phase (56), in agreement with studies by Yamada et al. (61) and Even et al. (45) but in contrast with the higher value (29 meV) obtained by Sestu and colleagues (64).

In summary, a large variation exists in the exciton binding energies extracted for $MAPbI_3$, as listed in **Table 1**. However, a consensus appears to be emerging that E_b varies with temperature, and as such, a global value for E_b cannot be stated. Whereas the reduced effective mass m_r^* of the electron-hole system was found to change little upon the phase transition near 160 K (56), ϵ is a strong function of both frequency (55, 77) and temperature (36, 41), which will affect E_b according to Equation 1. The polarity of the MA cation along the direction of the C–N bond modifies the low-frequency values of the dielectric function with respect to that expected for hybrid perovskites with nonpolar cations and creates a dependence on the ensemble cation orientation (49, 50). Therefore, the thermal activation of the tumbling motion of the MA cation at ~160 K (see Section 2.1) is expected to induce strong changes in E_b with temperature. Consequently, a relatively smooth variation of ϵ was observed for $MAPbI_3$ in the gigahertz frequency range (36), whereas step-like changes near the phase transitions were measured for the near-static value of ϵ (41). As a result, a combination of a gradual change in E_b with increasing temperature and a sudden drop upon the phase transition near 160 K into the HT phase ought to be expected. Most studies allowing for such temperature variations (45, 56, 61, 64) present a picture of a low exciton binding energy at room temperature of at most a few tens of milli-electron volts, in agreement with earlier investigations of charge-carrier dynamics postulating the presence of just one photoexcited species, free charge carriers, in $MAPbI_3$ at room temperature (32, 33, 72).

3. EARLY-TIME RELAXATION DYNAMICS OF PHOTOGENERATED CHARGE CARRIERS

Absorption of sunlight by a perovskite sensitizer in a photovoltaic application will initially create electron-hole pairs with energy significantly above the band edge. In the early stages, the excited charge-carrier distribution will be out of equilibrium and subsequently relax through a range

of different processes toward the band edge. The mechanisms involved in such initial charge-carrier relaxation are well documented for typical inorganic semiconductors such as GaAs and have been the subject of numerous textbooks (e.g., 74, chapter 20; 84, chapter 7; 85, chapters 3–5). Hybrid lead halide perovskites have shown many of the hallmarks of typical direct inorganic semiconductors, such as low exciton binding energies (see Section 2.2) and high charge-carrier mobilities (32, 86). Therefore, many of the descriptions developed, for example, for GaAs are likely to be of relevance here, although analogous investigations for hybrid metal halide perovskites are still at an incipient stage. Below, a brief listing is provided of the initial charge-carrier relaxation pathways established for classical inorganic semiconductors, followed by a summary of the current state of investigations for hybrid metal halide perovskites.

1. **Loss of coherence.** For excitation with coherent laser light, the generated polarization in the medium originating from photoexcited electron-hole pairs may initially maintain a fixed phase relationship or coherence between different photogenerated states and/or with the original laser pulse. Such coherence is subsequently lost through scattering events, for example, through collisions with charge carriers or phonons (85, chapters 3–5).
2. **Charge-carrier thermalization.** Immediately following nonresonant photoexcitation, the charge-carrier distribution inside the semiconductor will be nonthermal; that is, it cannot be described by any given electron temperature. This initially generated nonequilibrium distribution of charge carriers will rapidly (less than or equal to picoseconds) relax within the electronic bands (see **Figure 2**) through carrier scattering and establish a thermalized Maxwell distribution characterized by a carrier temperature T_c (85, chapters 3–5).
3. **Charge-carrier cooling.** While the charge-carrier temperature T_c is elevated above the lattice temperature T_L, carriers are described as hot. Subsequent carrier cooling is established through interactions with the lattice (85, chapters 3–5). For typical bulk inorganic semiconductors, an initial rapid carrier-cooling rate is observed that derives from interactions between the longitudinal optical (LO) phonon population with the electron and hole densities (87, 88). A subsequent slower cooling derives from thermal equilibrium being reestablished between LO and acoustic phonons, which may, for example, occur through zone-center decay of LO phonons into counterpropagating acoustic phonons. However, for elevated excitation densities, the LO phonon mode occupation may increase and the acoustic phonon bath temperature may be raised toward the charge-carrier temperature, causing significant phonon reabsorption that keeps charge carriers hot for an extended time period (phonon bottleneck) (88, 89). An understanding of the timescales involved in charge-carrier cooling is particularly interesting in the context of photovoltaics: While charge carriers are hot, such excess energy can in principle be harvested at charge-extracting contacts, yielding higher open-circuit voltages and PCEs. The study of charge-carrier cooling therefore presents an interesting opportunity in the context of perovskite sensitizers.
4. **Band-gap renormalization, Fermi filling, and the Mott transition.** For high charge-carrier densities following intense excitation of a semiconductor, charge-carrier dynamics are usually influenced by many-body and state-filling effects, which leave a signature in the dynamic spectra. Band-gap renormalization leads to a red shift of the band edge as a result of exchange and correlation effects. Here, the Pauli principle prevents two electrons with identical spin from occupying the same unit cell (exchange energy), whereas the Coulombic repulsion maximizes the distance between like charges in space (correlation energy). The resulting energy minimization becomes sizable for high charge-carrier densities, leading to a lowering or red shift of the band-gap energy (74, chapter 20). Conversely, state-filling or Burstein-Moss (90, 91) effects lead to a blue shift of the perceived band gap with increasing charge-carrier density because of the finite density of states available for occupation to the

fermionic electrons. Additional complications will arise if excitonic effects are to play a role, as excitonic features will be broadened through scattering at higher charge-carrier densities and are expected to be fully screened above the Mott density (74, chapter 20).

Studies of the initial charge-carrier relaxation dynamics in hybrid metal halide perovskites have so far almost exclusively focused on thin films of $MAPbI_3$ as a prototypical material (14, 63, 92–100). Here, the technique most commonly used for observation of charge-carrier relaxation has been transient absorption measurements with sub-100-fs pulses, which offer information through an analysis of recorded spectral dynamics. Early investigations have therefore often centered on the interpretation of such photoinduced absorption spectra, with two main discussion points being the precise shape of the spectra around the band edge (63, 92, 93, 99, 100) (near 760 nm, or 1.6 eV) and the origin of an observed high-energy peak (92, 93) near 480 nm (2.6 eV).

Given the correspondence between the **high-energy photoinduced absorption feature** of $MAPbI_3$ at 480 nm (2.6 eV) and the secondary onset observed in linear absorption spectra (**Figure 2**), many studies have postulated a common origin (45, 92, 93, 96). Although Sum and coworkers (92) assigned the higher-energy feature to a VB2 → CB1 transition between electronic bands, Kamat and coworkers (93, 94, 101) attributed it to a charge-transfer band. Further complexity was found to arise when residual PbI_2 precursor was present in the film, as the band-edge absorption onset of PbI_2 was associated with an additional photobleaching signal near 510 nm that overlapped with the high-energy feature observed for $MAPbI_3$ (95). The two parallel strands of discussion currently present in the literature with regard to the high-energy (480 nm) photoinduced absorption feature in $MAPbI_3$, evoking explanations either in terms of electronic band structure (14, 92, 96–98) or in terms of electronic states associated with different ionic lead halide complexes (93, 94, 101), may to some extent be equivalent, given that electronic bands originate from different atomic orbital contributions. Even et al. (45) and Kawai et al. (96) evaluated the strengths of the dipole-allowed transitions VB2 → CB1 and VB1 → CB2 at the *R* point (**Figure 2**) and found that these were partly dipole-allowed, but substantially lower in oscillator strength than the VB1 → CB1 transition at the *M* point. Further research is therefore needed to ascertain the precise origin of such high-energy absorption features and the factors (potentially interband relaxation) that govern the relaxation of charge-carriers in the associated states.

In addition, many studies (14, 63, 92, 93, 97–100) focused on an analysis of **photoinduced absorption features near the band edge** (1.6 eV), with the exact explanation for the observed spectral shape still a matter of debate. While some researchers attributed the photoinduced band-edge features to a combination of excitonic and free-charge-carrier effects (63, 100), others showed that a combination of solely free-charge-carrier effects and modulations of the refractive index could suffice to reproduce the spectra (99). Thus, the multitude of photoinduced relaxation mechanisms itemized above and the combination of both induced transmission and reflection changes lead to a complex evolution of the transient spectra near the band edge.

Despite such open questions about the exact shape of the photoinduced absorption spectra, there is general consensus that signals somewhat above the band edge (>1.7 eV) are caused by the presence of hot charge carriers. Early studies investigating the **dynamics of hot charge carriers** from transients in this spectral region (14, 92, 97, 98) generally reported fast, subpicosecond initial charge-carrier cooling dynamics. However, these short-lived dynamics were often superimposed to varying degrees onto longer-lived (10–1000 ps) dynamics even for probes energetically substantially above the band edge (92, 93, 98). A recent study by Kawai et al. (96) elucidated the origin of the fast, subpicosecond charge-carrier cooling component through DFT calculations. This study suggested that, similar to the case of GaAs and many other inorganic semiconductors (85, chapters 3–5), the initial fast carrier cooling proceeds mainly through coupling to LO phonon

modes (here associated with the lead-iodide lattice) (96). This relaxation pathway seems sensible given that such lead halide vibrational modes have been shown to couple to the photoinduced charge-carrier density, leaving their signature in photoconductivity spectra (32, 78). Kawai et al. proposed that hot-carrier relaxation is mainly limited by hole cooling, which they calculated to slow in the spectral region of 0.6 eV above the VBM1 as a result of the calculated narrow density of states they evaluated for that region, leading to cooling times in the picosecond region. More detailed experimental studies have subsequently extracted charge-carrier temperatures as a function of time after nonresonant excitation and reported a marked slow-down of cooling rates for higher excitation densities (63, 99) attributed to a phonon bottleneck, as described above. High-fluence excitation with short pulses derived from amplified laser systems may easily drive the system into the regime of a phonon bottleneck in which charge carriers are kept hot for an extended period (88, 89) because of high phonon occupancy. However, the extent to which hot charge carriers can actually be harvested under much less intense solar (AM1.5) illumination in a suitable photovoltaics device structure still needs to be examined.

Many-body and state-filling effects in transient spectra have so far received less explicit attention than carrier cooling dynamics. Manser & Kamat (93) reported a blue shift in the photobleaching peak of the spectral feature associated with the VB1 → CB1 transition at the *R* point for $MAPbI_3$, which they attributed to the Burstein-Moss shift arising from Fermi-level filling. Values for the dynamic Burstein-Moss shift were extrapolated from the width of the photobleach signal, although underlying hot-carrier and band-gap renormalization effects were, as a first approximation, excluded from the analysis. Later studies have interpreted the complex transient absorption lineshape around the band edge in terms of bandgap renormalization, Burstein-Moss effects, and charge-carrier cooling (63, 99). However, the conducting-to-insulating Mott transition arising from the screening of the Coulombic interactions between charge-carrier pairs at high densities has not yet been examined through direct experiments. As Section 2.2 suggests, such experiments may have to be conducted at low temperature for which excitons are more likely to be present following photoexcitation. Although high-density effects may be of relatively scant relevance to the use of hybrid metal halide perovskites in photovoltaics applications, they are likely to have a strong effect in devices requiring high charge injection densities, such as light-emitting diodes and lasers for which energetic shifts may cause instabilities arising from cavity and interface design.

Finally, the extent to which **electronic coherences** can be maintained following photoexcitation of $MAPbI_3$ has not received any attention to date. Given the significant coupling of electronic transitions to the lattice in this material class, coherence times may not necessarily be any higher than those found for typical inorganic semiconductors. However, such investigations may yield general insights into the fundamental properties of these materials, for example, through observations of coherent electron-phonon coupling, coherent control, or quantum beating, allowing potential identification of narrowly split band states (85, chapters 3–5).

4. CHARGE-CARRIER RECOMBINATION DYNAMICS

Charge-carrier recombination mechanisms and the resulting dynamics play a fundamental role in the functioning of semiconducting materials in electronic devices. For solar cells, the charge-carrier lifetime limits the time available to extract charges to contacts before competing recombination occurs, making it one of the most examined parameters. Wehrenfennig et al. (32) pointed out early that hybrid lead halide perovskites are highly effective materials for photovoltaics because they combine the best of both worlds: high charge-carrier mobilities and low charge-carrier recombination rates. The study utilized combined time-resolved terahertz photoconductivity and photoluminescence measurements to examine the decay of a free-charge-carrier density $n(t)$ in

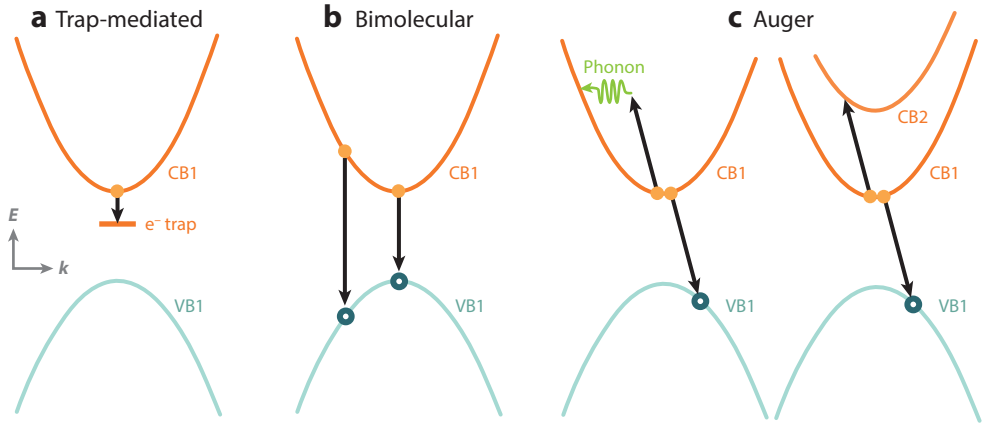

Figure 3

Schematic diagram indicating recombination mechanisms active in organic-inorganic metal halide perovskites. (*a*) Trap-assisted recombination is a monomolecular process involving the capture of either an electron (as shown) or a hole in a specific trap state (e.g., defect). (*b*) Bimolecular recombination may occur between electrons and holes, from either the relaxed state (CBM → VBM) or states higher in the band. (*c*) Auger recombination is a higher-order process involving at least three particles. The energy of an electron (or hole) is here transferred to another electron (or hole) to allow nonradiative recombination with a hole (or electron). As indicated, all processes have to satisfy energy and momentum conservation. Abbreviations: CB, conduction band; CBM, conduction band minimum; VB, valence band; VBM, valence band maximum.

terms of different contributing mechanisms, as expressed through the rate equation

$$\frac{\mathrm{d}n}{\mathrm{d}t} = -k_3 n^3 - k_2 n^2 - k_1 n. \tag{2}$$

Here, k_1 is the rate constant associated with monomolecular recombination, which may be due to excitonic recombination (assuming the two-particle state is already formed) or trap-assisted recombination that relies on an individual carrier (electron or hole) being captured in a trap (see **Figure 3*a***). The bimolecular charge-carrier recombination rate constant k_2, conversely, reflects intrinsic electron-hole recombination (see **Figure 3*b***), which depends on both electron (n_e) and hole (n_h) densities and therefore on $n_e n_h = n^2$ for photoexcitation. Finally, Auger recombination (102) is a many-body process that involves recombination of an electron with a hole, accompanied by energy and momentum transfer to a third participant, either an electron or a hole, potentially also involving phonon absorption or emission (see **Figure 3*c***). The resulting Auger recombination is strongly dependent on the charge-carrier density and is described by the Auger rate constant k_3. Taken together, the three recombination mechanisms contribute to the total recombination rate $r(n, t)$, which in turn influences the charge-carrier diffusion length L_D according to

$$r(n) = k_3 n^2 + k_2 n + k_1, \qquad L_\mathrm{D}(n) = \sqrt{\frac{\mu k_\mathrm{B} T}{r(n) e}}, \tag{3}$$

where μ is the charge-carrier mobility, T is the temperature, k_B is the Boltzmann constant, and e is the elementary charge (32, 78).

Such distinction between different mechanisms is crucial when charge-carrier recombination dynamics are analyzed, for several reasons. First, the differences in origin of these mechanisms mean that highly specific strategies are needed to alter any given rate. Second, the relative importance of the three contributions will vary depending on the device application, such as solar cells or light-emitting diodes and lasers.

For solar cells under AM1.5 illumination, typical charge-carrier concentrations are relatively low (10^{15}–10^{16} cm^{-3}, (86)); hence, much focus has been devoted to reducing the density of trap states (and therefore k_1) through variations in processing conditions (28, 33, 103–105). As Equation 2 shows, a decrease in k_1 will increase the charge-carrier diffusion length L_D (in particular, in the low-density regime), facilitating the use of planar heterojunction device architectures when L_D exceeds the absorption depth of sunlight in the perovskite absorber layer.

For light-emitting applications (e.g., light-emitting diodes and lasers), in particular, the important question is which recombination mechanism gives rise to light emission. Because no clear spectral signature for trap-mediated fluorescence has been observed for hybrid lead halide perovskites, and studies mostly point to an absence of excitonic effects at room temperature, k_1 should be associated with predominantly nonradiative recombination. In contrast, bimolecular recombination should be predominantly radiative for these direct semiconductors. Finally, Auger recombination is inherently nonradiative given that energy and momentum are used for intra- or interband transitions and will mostly be lost in heat. As a result, light emission from these materials should be particularly effective for the "sweet spot" in charge-carrier density at which the bimolecular recombination rate $k_2 n$ dominates over both monomolecular (k_1) and Auger ($k_3 n^2$) rates (86). This effect has indeed been observed for $MAPbI_3$: Saba et al. (62) found that the photoluminescence quantum efficiency peaked near a charge-carrier density of $\sim 10^{18}$ cm^{-3}, in agreement with earlier analysis of recombination mechanisms, which found that bimolecular recombination dominates in the charge-carrier density range 10^{17}–10^{18} cm^{-3}(32). Similarly, the photoluminescence intensity of $MAPbI_3$ increased superlinearly (72) and the efficiency of light-emitting diodes based on $MAPbI_3$ (11) increased toward the bimolecular recombination regime. An investigation of the diode ideality factor confirmed that, whereas trap-assisted recombination was mainly nonradiative, bimolecular recombination was mostly radiative (12). Efficient light-emitting devices will therefore need to operate at injected charge-carrier densities above present trap densities (82) but below the regime for which Auger recombination becomes dominant (32, 86). It should also be stressed that for photovoltaic applications, radiative recombination is not necessarily detrimental as the reverse process of light absorption leads to efficient harvesting of solar radiation. Given these considerations, the properties and origin of each of the presented recombination mechanisms are discussed separately below.

4.1. Trap-Assisted (Monomolecular) Recombination

A reduction in the trap density has been a primary goal in the area of perovskite photovoltaics, with a host of different processing techniques under development (28, 33, 103–105). Given the focus of this review on the fundamental properties of hybrid metal halide perovskites, there is insufficient space to give justice to the wide range of different approaches here. However, it is easy to see that the inherently strong dependence of trap-induced recombination on trap types, energetics, and densities will impart a strong dependence on processing conditions. Not surprisingly, a wide range of monomolecular charge-carrier lifetimes $\tau_1 = k_1^{-1}$ has been reported for thin films of $MAPbI_3$ and $MAPbI_{3-x}Cl_x$, ranging from 4 ns to $\sim$1 μs (corresponding to $k_1 = 1$–250×10^6 s^{-1}) (28, 33, 62, 72, 92, 103, 105–107). Given the high charge-carrier mobilities of approximately 8–70 $cm^2(Vs)^{-1}$ reported for $MAPbI_3$ and $MAPbI_{3-x}Cl_x$ films (32, 34, 78, 106), it is not surprising that large charge-carrier diffusion lengths have been found, ranging from 100 nm to several micrometers (31–33, 78, 92, 104, 108–110) at room temperature in the low charge-carrier density regime.

In addition, strong material specificity can be expected for trap-related recombination channels given that the nature of the traps will vary with elemental composition. For $MASnI_3$ infused into a mesoporous metal oxide layer, a value of $k_1 = 8 \times 10^9$ s^{-1} has been reported, which is orders

of magnitude above values typically found for $MAPbI_3$ (24). This effect has been attributed to fast recombination of electrons with a high density of p-type charge carriers resulting from self-doping in the presence of Sn^{4+} (24). For mixed iodide-bromide perovskite systems such as $MAPbBr_yI_{3-y}$ and $FAPbBr_yI_{3-y}$, the monomolecular rate was strongly linked with crystal morphology, with k_1 increasing substantially toward the central ($y/3 = 0.3$–0.5) region (111, 112), where these materials exhibit poor crystallinity as a result of changes in their crystal structure (22). However, it has recently been shown that such effects can be overcome through judicious choice of mixed inorganic (Cs) and organic (FA) A cations, which allows formation of stable lead mixed iodide-bromide perovskites (113).

While trap-related charge-carrier recombination has thus been examined in some detail, concrete knowledge of the exact nature of trap states in hybrid metal halide perovskites is still emerging. The subsections below summarize reported findings on the nature and distribution of trap states for the most frequently examined materials: $MAPbI_3$ and $MAPbI_{3-x}Cl_x$.

4.1.1. Nature of defect states. Yin et al. (114) and Kim et al. (115) recently presented DFT simulations of potential defect states in $MAPbI_3$. Both studies concluded that the most prominent defect states have only shallow trap depths, in accordance with the favorable charge-transport properties of the material. Elemental vacancies (i.e., missing lead, iodine, or MA) were considered in both studies to be likely candidates, with shallow trap levels (115) of trap depths below 50 meV (114). Yin et al. also highlighted a correlation between trap depth and the associated formation energy; that is, deep (few hundred milli-electron volt) traps fortunately appear to be much harder to introduce (114).

Experimental evidence on the nature and depth of traps is rather diverse, as might be expected given that processing conditions vary largely across the field. De Wolf et al. (116) reported absorption onsets with an Urbach tail of 15 meV for $MAPbI_3$, and no deep traps could be found. Oga et al. (106) also reported shallow traps on the order of 10 meV, extracted from modeling of photoconductivity spectra. Wu et al. (117), conversely, proposed a broad range of subgap states 100–400 meV below the band edge; however, charge-carrier lifetimes reported in the study were relatively low (few nanoseconds), suggesting materials with high trap density. Milot et al. (44) recently reported that the monomolecular charge recombination rate for $MAPbI_3$ increases with increasing temperature between 8 and 350 K, which could derive from a charge-recombination process assisted by ionized impurities. As the temperature is reduced below the ionization energy associated with the impurity, the released electrons or holes return, effectively passivating these sites. An effective trap depth of 20 meV was extracted for the RT tetragonal phase (44), in good agreement with calculations by Yin et al. (114). However, the activation energy increased to ≈200 meV above ≈310 K in the cubic phase, suggesting that relative trap energies are linked with the crystal structure (44).

4.1.2. Trap densities and spatial distribution. The trap density in thin films of $MAPbI_3$ and $MAPbI_{3-x}Cl_x$ processed from typical solution routes has been examined through a wide range of techniques, with reported values in the range 10^{16}–10^{17} cm^{-3} (13, 82, 93, 118). For single crystals with volume exceeding 100 mm^3, conversely, much lower trap densities of 10^9–10^{10} cm^{-3} were found. There is mounting evidence that trap densities may be significantly larger near grain boundaries or at interfaces (13, 28, 103), making trap-related recombination also a function of crystallite size. The spatial distribution of trap states complicates the description of trap-related recombination through a simple time constant k_1, as given in Equation 2. If trap distributions are spatially inhomogeneous, rate equations have to be augmented with diffusion terms [e.g., $D\nabla^2 n(x, y, z, t)$ (33, 110)] and solved under consideration of the spatial trap distribution. In addition, trap

saturation may have to be accounted for separately, which slows trap-assisted recombination when charge-carrier densities reach the density of unoccupied trap states (82). Such effects lead to deviations of charge-carrier density decays from simple exponential behavior [$n = n_0 \exp(-k_1 t)$] and are sometimes accounted for by a description with a stretched exponential function [i.e., $n = n_0 \exp(-t/\tau)^{\beta}$ (28, 33)], which is equivalent to a time-dependent monomolecular recombination rate, $k_1(t) = \beta \tau^{-\beta} t^{\beta-1}$ (119).

4.2. Bimolecular (Electron-Hole) Recombination

Bimolecular recombination sets a fundamental intrinsic limit to charge-carrier diffusion lengths once trap-assisted recombination channels have been eliminated (see Equation 3). Wehrenfennig et al. (32) highlighted that the ratio of the bimolecular recombination constants k_2 of $MAPbI_3$ and $MAPbI_{3-x}Cl_x$ ($\sim 10^{-10}$ $cm^3 s^{-1}$) to the charge-carrier mobility μ (~ 10 $cm^2 V^{-1} s^{-1}$) was exceptionally low, a scenario that defied the Langevin limit by at least four orders of magnitude. The simple Langevin model establishes a predicted ratio of $k_2/\mu = e/(\epsilon_0 \epsilon_r)$ under the assumption that recombination will occur once an electron and a hole move within their joint capture radius, which is presumed to be larger than their mean free path (71, 120). While low radiative bimolecular recombination by itself may not be an aim for photovoltaic materials because it could also lower absorption coefficients, materials with k_2/μ ratios that fall substantially short of the Langevin limit are highly desirable, as they allow for long charge-carrier diffusion lengths, L_D (see Equation 3). It has been shown that if bimolecular rate constants adhered to the prediction of Langevin theory, $L_D \sim 100$ nm would be expected for $MAPbI_{3-x}Cl_x$ (as opposed to an actual value of 3 μm) (78), making non-Langevin recombination a crucial prerequisite for solar cells based on a planar heterojunction architecture (121). The bimolecular recombination constant for $MAPbI_3$ and $MAPbI_{3-x}Cl_x$ has now been measured repeatedly through a range of spectroscopic techniques (32, 44, 59, 72, 78, 93, 97, 107, 110), generally yielding values in the range $\sim 0.8–20 \times 10^{-10}$ $cm^3 s^{-1}$. Variations in the reported value of k_2 are hence significantly smaller than for trap-related recombination (k_1), which presumably reflects the more intrinsic nature of the bimolecular recombination mechanism. Interestingly, such low (non-Langevin) ratios of bimolecular recombination rate constants to mobilities have also been determined for $MASnI_3$ (24) and the $FAPbBr_yI_{3-y}$ material system (112), suggesting that this is a more general positive feature of hybrid metal halide perovskites.

Several recent studies have examined the non-Langevin bimolecular recombination mechanism in these materials (32, 59, 78, 94, 122). Recombination rate constants below the Langevin limit have been observed in other low-mobility materials that have been successfully incorporated into photovoltaic cells. For solution-processed demixed blends of conjugated polymer with fullerene derivatives (123–125), such effects have been attributed to electrons and holes being separated into two material components. For amorphous silicon (126), spatial charge separation through the presence of a random potential landscape has been evoked. Such comparison triggered suggestions that the electronic structure of hybrid metal halide perovskites may similarly induce an intrinsic spatial charge separation that reduces recombination rates (32). As discussed in Section 2.1.2, density-functional calculations on lead-iodide perovskites have revealed that VBM consist of 6s and 5p orbitals of lead and iodine, respectively, whereas CBM mostly incorporate 6p orbitals of lead. It was therefore proposed that a weak preferential localization of electrons and holes in different regions of the perovskite unit cell may cause a reduction in the spatial overlap of electron and hole wave functions and hence recombination rates (32), as demonstrated in recent DFT calculations of spatial charge density distributions near the VBM and CBM of $MAPbI_3$ (122). Accordingly, Manser and colleagues (94) and Kamat and colleagues (101) proposed that

electronic excitations at different energies may access parts of the electronic state structure that have different charge-transfer character.

Savenije et al. (59) examined the temperature dependence in the range 160–300 K of the bimolecular recombination constant extracted through fitting to microsecond transient microwave conductivity transients. The value of k_2 was found to decrease (by a factor of ~7) with decreasing temperature, which the authors attributed to second-order recombination in $MAPbI_3$ requiring an activation energy of 75 meV as a result of MA cation rotation participating in the charge recombination mechanism. However, Milot et al. (44) found opposite trends in a study of k_2 determined from nanosecond terahertz conductivity measurements conducted between 8 and 360 K. Here, a substantial increase in k_2 was found with decreasing temperature. This effect was linked to an observed increase in charge-carrier mobility with decreasing temperature (44), which had previously been attributed to reduced electron-phonon scattering (59, 106). As a result, the approach velocity into the joint Coulomb potential of the electron and hole may be increased with decreasing temperature, enhancing bimolecular recombination (44). However, an alternative explanation may arise from considering electronic band structure. As the temperature is reduced, the thermal occupation near the band edge sharpens, leading to an increase in band-to-band recombination (86).

Deviations from Langevin's predictions have often served as an excellent benchmark for identifying materials that are particularly suitable for photovoltaic applications (32, 125, 126). However, a better understanding of bimolecular recombination in hybrid metal halide perovskites clearly requires the consideration of alternative models, derived from, e.g., the electronic bandstructure, that yield an accurate reflection of the experimentally observed rates.

4.3. Many-Body (Auger) Recombination

Nonradiative Auger recombination in hybrid metal halide perovskites has been examined to a lesser extent, possibly because of the high excitation fluences required to monitor such effects. Reported Auger rate constants k_3 vary in the range $0.2–10 \times 10^{-28}$ cm^6s^{-1} for $MAPbI_3$ and $MAPbI_{3-x}Cl_x$ (32, 44, 78, 97, 110), suggesting that Auger recombination is unlikely to operate in photovoltaic devices under standard sunlight, although it may become relevant for operation of perovskite photovoltaics in solar concentrator settings. In addition, Auger effects are important for the implementation of hybrid perovskites in lasers, which operate in the high charge-density regime (13–16). Onsets of amplified stimulated emission have been reported to occur at excitation pulse fluences of 7–70 μJ cm^{-2} in thin films of $MAPbI_3$, corresponding to peak charge-carrier densities of $1–10 \times 10^{18}$ cm^{-3} for the given scenarios (13–15). The use of Equation 3 reveals that for a parameter set of $k_1 = (300\ ns)^{-1}$, $k_2 = 10^{-10}$ cm^3s^{-1}, and $k_3 = 10^{-28}$ cm^6s^{-1} typical for high-quality $MAPbI_3$ films, the Auger recombination rate k_3n^2 already contributes 50–90% to the overall rate $r(n)$ at these charge-carrier densities (86). A better understanding of factors affecting Auger mechanisms is therefore urgently needed to facilitate the design of materials with lower nonradiative losses in the high-density regime.

In general, Auger rates in semiconductors are highly influenced by the requirement of overall energy and momentum conservation in the many-body process (102) (see **Figure 3*c***). One consequence is a high dependence of the Auger rate on the electronic band structure (127, 128). In addition, Auger recombination may be affected by impurities and, as **Figure 3*c*** illustrates, by phonons that assist by accepting or donating momentum (129, 130). Efficient Auger recombination often results from the involvement of split-off bands that facilitate energy and wave-vector conservation (127). Even et al. (40) proposed that in $MAPbI_3$ such mechanisms differ subtly from those in traditional semiconductors such as GaAs because of the reverse ordering of the band structure,

which means that split-off and light/heavy electron conduction bands would be involved rather than the equivalent valence bands as in the case of GaAs.

Experimental evidence on how Auger rate constants may change with the band structure of hybrid metal halide perovskites is only just emerging. Milot et al. (44) demonstrated that Auger rate constants in $MAPbI_3$ exhibit exceptionally strong structural phase specificity, falling with increasing temperature in the orthorhombic phase (8–160 K), rising in the tetragonal phase (160–315 K), and falling again as the temperature is raised above 315 K in the cubic phase. In addition, Rehman et al. (112) showed that the Auger rate constant for the mixed iodide-bromide perovskite system $FAPbBr_yI_{3-y}$ increased monotonously by an order of magnitude when the bromide fraction $y/3$ was increased from 0 to 1, which coincides with the occurrence of gradual changes in the pseudocubic lattice parameter (22). Such dependence of Auger rates on the underlying crystal structure confirms the expected link with electronic and/or vibrational structure. These early experiments suggest that suitable band-structure engineering (e.g., through changes in organic cation size) has the potential to dramatically reduce these rates. A detailed theoretical analysis of what constitutes Auger mechanisms in these materials is therefore urgently needed for the design of hybrid metal halide materials for efficient lasing applications.

5. CONCLUDING REMARKS

In summary, organic-inorganic metal halide perovskites have proven to be a fascinating material system to investigate. Few materials show such inherent flexibility in terms of compositional and structural modification, yet allow for excellent optoelectronic properties, including high charge-carrier mobilities, strong optical absorption, and low trap-assisted recombination rates. Whether perovskite photovoltaic cells will become competitors to current silicon technology, the lessons learned from investigating their photophysics will serve as highly valuable guidelines on how to design effective light-harvesting and light-emitting materials.

SUMMARY POINTS

1. Hybrid organic-inorganic metal halide perovskites exhibit interesting structure-property relationships deriving from their propensity to undergo structural transformations with relative ease.
2. The exciton binding energy E_b appears to be a function of temperature as a result of the strong temperature dependence of the dielectric function. At room temperature, E_b is in the range of a few milli-electron volts to at most a few tens of milli-electron volts, in accordance with the presence of a free-charge-carrier population.
3. Charge-carrier relaxation dynamics within the first few picoseconds after excitation are marked by thermalization, cooling, and many-body effects. It remains to be explored whether extended hot charge-carrier phases can be utilized in photovoltaic devices that exceed the Shockley-Queisser limit.
4. Trap-assisted (monomolecular) charge-carrier recombination is mostly nonradiative and highly specific to material processing, yielding associated lifetimes from nano- to microseconds. Traps in hybrid lead halide perovskites appear to be mostly shallow (approximately tens of milli-electron volts), arising, for example, from elemental metal, halide, or organic vacancies, and may be present in higher density near interfaces and grain boundaries.

5. Bimolecular charge-carrier recombination is predominantly radiative and exhibits rate constants that defy the Langevin limit by many orders of magnitude.
6. Nonradiative Auger recombination is significant for charge-carrier densities corresponding to the threshold for amplified spontaneous emission. Rate constants show a strong specificity to crystal structure, opening the possibility for the design of materials with low Auger rates from first-principles calculations.

DISCLOSURE STATEMENT

The author is not aware of any affiliations, memberships, funding, or financial holdings that might be perceived as affecting the objectivity of this review.

ACKNOWLEDGMENTS

Financial support by the UK Engineering and Physical Sciences Research Council (EPSRC) is gratefully acknowledged.

LITERATURE CITED

1. Green MA, Emery K, Hishikawa Y, Warta W, Dunlop ED. 2015. Solar cell efficiency tables (Version 45). *Prog. Photovolt. Res. Appl.* 23:1–9
2. Kojima A, Teshima K, Shirai Y, Miyasaka T. 2009. Organometal halide perovskites as visible-light sensitizers for photovoltaic cells. *J. Am. Chem. Soc.* 131:6050–51
3. Lee MM, Teuscher J, Miyasaka T, Murakami TN, Snaith HJ. 2012. Efficient hybrid solar cells based on meso-superstructured organometal halide perovskites. *Science* 338:643–47
4. Kim HS, Lee CR, Im JH, Lee KB, Moehl T, et al. 2012. Lead iodide perovskite sensitized all-solid-state submicron thin film mesoscopic solar cell with efficiency exceeding 9%. *Sci. Rep.* 2:591
5. Ball JM, Lee MM, Hey A, Snaith HJ. 2013. Low-temperature processed meso-superstructured to thin-film perovskite solar cells. *Energy Environ. Sci.* 6:1739–43
6. Liu M, Johnston MB, Snaith HJ. 2013. Efficient planar heterojunction perovskite solar cells by vapour deposition. *Nature* 501:395–98
7. Chen Q, Zhou H, Hong Z, Luo S, Duan HS, et al. 2013. Planar heterojunction perovskite solar cells via vapor-assisted solution process. *J. Am. Chem. Soc.* 136:622–25
8. Burschka J, Pellet N, Moon SJ, Humphry-Baker R, Gao P, et al. 2013. Sequential deposition as a route to high-performance perovskite-sensitized solar cells. *Nature* 499:316–19
9. Yang WS, Noh JH, Jeon NJ, Kim YC, Ryu S, et al. 2015. High-performance photovoltaic perovskite layers fabricated through intramolecular exchange. *Science* 348:1234–37
10. Zhang Y, Liu M, Eperon GE, Leijtens T, et al. 2015. Charge selective contacts, mobile ions and anomalous hysteresis in organic-inorganic perovskite solar cells. *Mater. Horiz.* 2:315–22
11. Tan ZK, Moghaddam RS, Lai ML, Docampo P, Higler R, et al. 2014. Bright light-emitting diodes based on organometal halide perovskite. *Nat. Nanotechnol.* 9:687–92
12. Wetzelaer GJAH, Scheepers M, Sempere AM, Momblona C, Avila J, Bolink HJ. 2015. Trap-assisted non-radiative recombination in organic-inorganic perovskite solar cells. *Adv. Mater.* 27:1837–41
13. Xing G, Mathews N, Lim SS, Yantara N, Liu X, et al. 2014. Low-temperature solution-processed wavelength-tunable perovskites for lasing. *Nat. Mater.* 13:476–80
14. Chen K, Barker AJ, Morgan FLC, Halpert JE, Hodgkin JM. 2014. Effect of carrier thermalization dynamics on light emission and amplification in organometal halide perovskites. *J. Phys. Chem. Lett.* 6:153–58

15. Stranks SD, Wood SM, Wojciechowski K, Deschler F, Saliba M, et al. 2015. Enhanced amplified spontaneous emission in perovskites using a flexible cholesteric liquid crystal reflector. *Nano Lett.* 15:4935–41
16. Deschler F, Price M, Pathak S, Klintberg LE, Jarausch DD, et al. 2014. High photoluminescence efficiency and optically pumped lasing in solution-processed mixed halide perovskite semiconductors. *J. Phys. Chem. Lett.* 5:1421–26
17. Saliba M, Wood SM, Patel JB, Nayak PK, et al. 2016. Structured organic–inorganic perovskite toward a distributed feedback laser. *Adv. Mater.* 28:923–29
18. Gao P, Grätzel M, Nazeeruddin MK. 2014. Organohalide lead perovskites for photovoltaic applications. *Energy Environ. Sci.* 7:2448–63
19. Goldschmidt VM. 1926. Die Gesetze der Krystallochemie. *Die Naturwissenschaften* 21:477–85
20. Pena MA, Fierro JLG. 2001. Chemical structures and performance of perovskite oxides. *Chem. Rev.* 101:1981–2017
21. Glazer AM. 1972. The classification of tilted octahedra in perovskites. *Acta Cryst. B* 28:3384–91
22. Eperon GE, Stranks SD, Menelaou C, Johnston MB, Herz LM, Snaith HJ. 2014. Formamidinium lead trihalide: a broadly tunable perovskite for efficient planar heterojunction solar cells. *Energy Environ. Sci.* 7:982–88
23. US Geol. Surv. 2015. *Mineral commodity summaries 2015*. Rep., US Geol. Surv., Washington, DC
24. Noel NK, Stranks SD, Abate A, Wehrenfennig C, Guarnera S, et al. 2014. Lead-free organic-inorganic tin halide perovskites for photovoltaic applications. *Energy Environ. Sci.* 7:3061–68
25. Hao F, Stoumpos CC, Cao DH, Chang RPH, Kanatzidis MG. 2014. Lead-free solid-state organic-inorganic halide perovskite solar cells. *Nat. Photon.* 8:489–94
26. Noh JH, Im SH, Heo JH, Mandal TN, Seok SI. 2013. Chemical management for colorful, efficient, and stable inorganic-organic hybrid nanostructured solar cells. *Nano Lett.* 13:1764–69
27. Colella S, Mosconi E, Fedeli P, Listort A, Gazza F, et al. 2013. $MAPbI_{3-x}Cl_x$ mixed halide perovskite for hybrid solar cells: the role of chloride as dopant on the transport and structural properties. *Chem. Mater.* 25:4613–18
28. de Quilettes DW, Vorpahl SM, Stranks SD, Nagaoka H, Eperon GE, et al. 2015. Impact of microstructure on local carrier lifetime in perovskite solar cells. *Science* 348:683–86
29. Dar M, Arora N, Gao P, Ahmad S, Grätzel M, Nazeeruddin MK. 2014. Investigation regarding the role of chloride in organic-inorganic halide perovskites obtained from chloride containing precursors. *Nano Lett.* 14:6991–96
30. Mosconi E, Amat A, Nazeeruddin MK, Grätzel M, De Angelis F. 2013. First-principles modeling of mixed halide organometal perovskites for photovoltaic applications. *J. Phys. Chem. C* 117:13902–13
31. Edri E, Kirmayer S, Henning A, Mukhopadhyay S, Gartsman K, et al. 2014. Why lead methylammonium tri-iodide perovskite-based solar cells require a mesoporous electron transporting scaffold (but not necessarily a hole conductor). *Nano Lett.* 14:1000–4
32. Wehrenfennig C, Eperon GE, Johnston MB, Snaith HJ, Herz LM. 2014. High charge carrier mobilities and lifetimes in organo lead trihalide perovskites. *Adv. Mater.* 26:1584–89
33. Stranks SD, Eperon GE, Grancini G, Menelaou C, Alcocer MJP, et al. 2013. Electron-hole diffusion lengths exceeding 1 micrometer in an organometal trihalide perovskite absorber. *Science* 342:341–44
34. Stoumpos CC, Malliakas CD, Kanatzidis MG. 2013. Semiconducting tin and lead iodide perovskites with organic cations: phase transitions, high mobilities, and near-infrared photoluminescent properties. *Inorg. Chem.* 52:9019–38
35. Weber D. 1978. $CH_3NH_3PbX_3$, ein Pb(II)-System mit kubischer Perowskitstruktur. *Z. Naturforsch. B* 33:1443–45
36. Poglitsch A, Weber D. 1987. Dynamic disorder in methylammoniumtrihalogenplumbates (II) observed by millimeter-wave spectroscopy. *J. Chem. Phys.* 87:6373–78
37. Kawamura Y, Mashiyama H, Hasebe K. 2002. Structural study on cubic–tetragonal transition of $CH_3NH_3PbI_3$. *Phys. Soc. Jpn.* 71:1694–97
38. Baikie T, Fang Y, Kadro JM, Schreyer M, Wei F, et al. 2013. Synthesis and crystal chemistry of the hybrid perovskite $(CH_3NH_3)PbI_3$ for solid-state sensitised solar cell applications. *J. Mater. Chem. A* 1:5628–41

39. Wasylishen R, Knop O, Macdonald J. 1985. Cation rotation in methylammonium lead halides. *Solid State Commun.* 56:581–82
40. Even J, Pedesseau L, Katan C, Kepenekian M, Laurent J, et al. 2015. Solid-state physics perspective on hybrid perovskite. *J. Phys. Chem. C* 119:10161–77
41. Onada-Yamamuro N, Matsuo T, Suga H. 1992. Dielectric study of $CH_3NH_3PbX_3$ (X = Cl, Br, I). *J. Phys. Chem. Solids* 53:935–39
42. Onada-Yamamuro N, Matsuo T, Suga H. 1990. Calorimetric and IR spectroscopic studies of phase transitions in methylammonium trihalogenoplumbates (II). *J. Phys. Chem. Solids* 51:1383–95
43. Bakulin AA, Selig O, Bakker HJ, Rezus YLA, et al. 2015. Real-time observation of organic cation reorientation in methylammonium lead iodide perovskites. *J. Phys. Chem. Lett.* 6:3663–69
44. Milot RL, Eperon GE, Snaith HJ, Johnston MB, Herz LM. 2015. Temperature-dependent charge-carrier dynamics in $CH_3NH_3PbI_3$. *Adv. Funct. Mater.* 25:6218–27
45. Even J, Pedesseau L, Katan C. 2014. Analysis of multivalley and multibandgap absorption and enhancement of free carriers related to exciton screening in hybrid perovskites. *J. Phys. Chem. C* 118:11566–72
46. Wehrenfennig C, Liu M, Snaith HJ, Johnston MB, Herz LM. 2014. Homogeneous emission line broadening in the organo lead halide perovskite $CH_3NH_3PbI_{3-x}Cl_x$. *J. Phys. Chem. Lett.* 5:1300–6
47. Tanaka K, Takahashi T, Ban T, Kondo T, Uchida K, Miura N. 2003. Comparative study on the excitons in lead-halide-based perovskite-type crystals $CH_3NH_3PbBr_3$ $CH_3NH_3PbI_3$. *Solid State Commun.* 127:619–23
48. Even J, Pedesseau L, Jancu JM, Katan C. 2013. Importance of spin-orbit coupling in hybrid organic/inorganic perovskites for photovoltaic applications. *J. Phys. Chem. Lett.* 4:2999–3005
49. Brivio F, Walker A, Walsh A. 2013. Structural and electronic properties of hybrid perovskites for high-efficiency thin-film photovoltaics from first-principles. *APL Mater.* 1:042111
50. Frost JM, Butler KT, Brivio F, Hendon CH, van Schilfgaarde M, Walsh A. 2014. Atomistic origins of high-performance in hybrid halide perovskite solar cells. *Nano Lett.* 14:2584–90
51. Filip MR, Giustino F. 2014. GW quasiparticle band gap of the hybrid organic-inorganic perovskite $CH_3NH_3PbI_3$: effect of spin-orbit interaction, semicore electrons, and self-consistency. *Phys. Rev. B* 90:245145
52. Amat A, Mosconi E, Ronca E, Quarti C, Umari P, et al. 2014. Cation-induced band-gap tuning in organohalide perovskites: interplay of spin-orbit coupling and octahedra tilting. *Nano Lett.* 14:3608–16
53. Katan C, Pedesseau L, Kepenekian M, Rolland A, Even J. 2015. Interplay of spin-orbit coupling and lattice distortion in metal substituted 3D tri-chloride hybrid perovskites. *J. Mater. Chem. A* 3:9232–40
54. Hirasawa M, Ishihara T, Goto T, Uchida K, Miura N. 1994. Magnetoabsorption of the lowest exciton in perovskite-type compound $(CH_3NH_3)PbI_3$. *Physica B* 201:427–30
55. Lin Q, Armin A, Nagiri RCR, Burn PL, Meredith P. 2015. Electro-optics of perovskite solar cells. *Nat. Photon.* 9:106–12
56. Miyata A, Mitioglu A, Plochocka P, Portugall O, Wang JTW, et al. 2015. Direct measurement of the exciton binding energy and effective masses for charge carriers in an organic-inorganic tri-halide perovskite. *Nat. Phys.* 11:582–87
57. D'Innocenzo V, Grancini G, Alcocer MJ, Kandada ARS, Stranks SD, et al. 2014. Excitons versus free charges in organo-lead tri-halide perovskites. *Nat. Commun.* 5:3586
58. Sun S, Salim T, Mathews N, Duchamp M, Boothroyd C, et al. 2014. The origin of high efficiency in low-temperature solution-processed bilayer organometal halide hybrid solar cells. *Energy Environ. Sci.* 7:399–407
59. Savenije TJ, Ponseca CS, Kunneman L, Abdellah M, Zheng K, et al. 2014. Thermally activated exciton dissociation and recombination control the carrier dynamics in organometal halide perovskite. *J. Phys. Chem. Lett.* 5:2189–94
60. Wu K, Bera A, Ma C, Du Y, Yang Y, et al. 2014. Temperature-dependent excitonic photoluminescence of hybrid organometal halide perovskite films. *Phys. Chem. Chem. Phys.* 16:22476–81
61. Yamada Y, Nakamura T, Endo M, Wakamiya A, Kanemitsu Y. 2015. Photoelectronic responses in solution-processed perovskite $CH_3NH_3PbI_3$ solar cells studied by photoluminescence and photoabsorption spectroscopy. *IEEE J. Photovoltaics* 5:401–5

62. Saba M, Cadelano M, Marongiu D, Chen F, Sarritzu V, et al. 2014. Correlated electron-hole plasma in organometal perovskites. *Nat. Commun.* 5:5049
63. Yang Y, Ostrowski DP, France RM, Zhu K, et al. 2016. Observation of a hot-phonon bottleneck in lead-iodide perovskite. *Nat. Photon.* 10:53–59
64. Sestu N, Cadelano M, Sarritzu V, Chen F, et al. 2015. Absorption f-sum rule for the exciton binding energy in methylammonium lead halide perovskites. *J. Phys. Chem. Lett.* 6:4566–72
65. Yan J, Saunders BR. 2014. Third-generation solar cells: a review and comparison of polymer:fullerene, hybrid polymer and perovskite solar cells. *RSC Adv.* 4:43286–314
66. Tang CW. 1986. Two-layer organic photovoltaic cell. *Appl. Phys. Lett.* 48:183–85
67. Yu G, Gao J, Hummelen JC, Wudl F, Heeger AJ. 1995. Polymer photovoltaic cells: enhanced efficiencies via a network of internal donor-acceptor heterojunctions. *Science* 270:1789–90
68. Bach U, Lupo D, Comte P, Moser JE, Weissortel F, et al. 1998. Solid-state dye-sensitized mesoporous TiO_2 solar cells with high photon-to-electron conversion efficiencies. *Nature* 395:583–85
69. Kersting R, Lemmer U, Deussen M, Bakker HJ, Mahrt RF, et al. 1994. Ultrafast field-induced dissociation of excitons in conjugated polymers. *Phys. Rev. Lett.* 73:1440–43
70. Knupfer M. 2003. Exciton binding energies in organic semiconductors. *Appl. Phys. A* 77:623–26
71. Pope M, Swenberg CE. 1999. *Electronic Processes in Organic Crystals and Polymers*. New York: Oxford Sci.
72. Yamada Y, Nakamura T, Endo M, Wakamiya A, Kanemitsu Y. 2014. Photocarrier recombination dynamics in perovskite $CH_3NH_3PbI_3$ for solar cell applications. *J. Am. Chem. Soc.* 136:11610–13
73. Ponseca CS, Savenije TJ, Abdellah M, Zheng K, Yartsev A, et al. 2014. Organometal halide perovskite solar cell materials rationalized: ultrafast charge generation, high and microsecond-long balanced mobilities and slow recombination. *J. Am. Chem. Soc.* 136:5189–92
74. Klingshirn CF. 1997. *Semiconductor Optics*. New York: Springer. 1st ed.
75. Dvorak M, Wei SH, Wu Z. 2013. Origin of the variation of exciton binding energy in semiconductors. *Phys. Rev. Lett.* 110:016402
76. Patel JB, Milot RL, Wright AD, Herz, LM et al. 2016. Formation dynamics of $CH_3NH_3PbI_3$ perovskite following two-step layer deposition. *J. Phys. Chem. Lett.* 7:96–102
77. Juarez-Perez AJ, Sanchez RS, Badia L, Garcia-Belmonte G, Kang YS, et al. 2014. Photoinduced giant dielectric constant in lead-halide perovskite solar cells. *J. Phys. Chem. Lett.* 5:2390–94
78. Wehrenfennig C, Liu M, Snaith HJ, Johnston MB, Herz LM. 2014. Charge-carrier dynamics in vapour-deposited films of the organolead halide perovskite $CH_3NH_3PbI_{3-x}Cl_x$. *Energy Environ. Sci.* 7:2269–75
79. Quarti C, Grancini G, Mosconi E, Bruno P, Ball JM, et al. 2014. The Raman spectrum of the $CH_3NH_3PbI_3$ hybrid perovskite: interplay of theory and experiment. *J. Phys. Chem. Lett.* 5:279–84
80. Perez-Osorio MA, Milot RL, Filip MR, Patel JB, et al. 2015. Vibrational properties of the organic–inorganic halide perovskite $CH_3NH_3PbI_3$ from theory and experiment: factor group analysis, first-principles calculations, and low-temperature infrared spectra. *J. Phys. Chem. C* 119:25703–18
81. Tvingstedt K, Malinkiewicz O, Baumann A, Diebel C, Snaith HJ, et al. 2014. Radiative efficiency of lead iodide based perovskite solar cells. *Sci. Rep.* 4:6071
82. Stranks SD, Burlakov VM, Leitens T, Ball JM, Goriely A, Snaith HJ. 2014. Recombination kinetics in organic-inorganic perovskites: excitons, free charge, and subgap states. *Phys. Rev. Appl.* 2:034007
83. Elliott RJ. 1957. Intensity of optical absorption by excitons. *Phys. Rev.* 108:1384–89
84. Yu PY, Cardona M. 1996. *Fundamentals of Semiconductors*. New York: Springer. 1st ed.
85. Shah J. 1999. *Ultrafast Spectroscopy of Semiconductors and Semiconductor Nanostructures*. New York: Springer. 1st ed.
86. Johnston MB, Herz LM. 2016. Hybrid perovskites for photovoltaics: charge-carrier recombination, diffusion and radiative efficiencies. *Acc. Chem. Res.* 49:146–54
87. von der Linde D, Lambrich R. 1979. Direct measurement of hot-electron relaxation by picosecond spectroscopy. *Phys. Rev. Lett.* 42:1090–93
88. Klimov V, Haring Bolivar P, Kurz H. 1995. Hot-phonon effects in femtosecond luminescence spectra of electron-hole plasmas in CdS. *Phys. Rev. B* 52:4728–31
89. Yong CK, Wong-Leung J, Joyce HJ, Lloyd-Hughes J, Gao Q, et al. 2013. Direct observation of charge-carrier heating at WZ-ZB InP nanowire heterojunctions. *Nano Lett.* 13:4280–87

90. Burstein E. 1954. Anomalous optical absorption limit in InSb. *Phys. Rev.* 93:632–33
91. Moss TS. 1954. The interpretation of the properties of indium antimonide. *Proc. Phys. Soc. B* 67:775–82
92. Xing G, Mathews N, Sun S, Lim SS, Lam YM, et al. 2013. Long-range balanced electron- and hole-transport lengths in organic-inorganic $CH_3NH_3PbI_3$. *Science* 342:344–47
93. Manser JS, Kamat PV. 2014. Band filling with free charge carriers in organometal halide perovskites. *Nat. Photon.* 8:737–43
94. Stamplecoskie KG, Manser JS, Kamat PV. 2015. Dual nature of the excited state in organic-inorganic lead halide perovskites. *Energy Environ. Sci.* 8:208–15
95. Wang L, McCleese C, Kovalsky A, Zhao Y, Burda C. 2014. Femtosecond time-resolved transient absorption spectroscopy of $CH_3NH_3PbI_3$ perovskite films: evidence for passivation effect of PbI_2. *J. Am. Chem. Soc.* 136:12205–8
96. Kawai H, Giorgi G, Marini A, Yamashita K. 2015. The mechanism of slow hot-hole cooling in lead-iodide perovskite: first-principles calculation on carrier lifetime from electron-phonon interaction. *Nano Lett.* 15:3103–8
97. Trinh MT, Wu X, Niesner D, Zhu X. 2015. Many-body interactions in photoexcited lead iodide perovskite. *J. Mater. Chem. A* 3:9285–90
98. Hsu H, Wang C, Fathi A, Shiu JW, Chung CC, et al. 2014. Femtosecond excitonic relaxation dynamics of perovskite on mesoporous films of Al_2O_3 and NiO nanoparticles. *Angew. Chem. Int. Ed.* 126:9493–96
99. Price MB, Butkus J, Jellicoe TC, Sadhanala A, et al. 2015. Hot-carrier cooling and photoinduced refractive index changes in organic–inorganic lead halide perovkites. *Nat. Commun.* 6:8429
100. Gancini G, Kandada ARS, Frost JM, Barker AJ, et al. 2016. Role of microstructure in the electron-hole interaction of hybrid lead halide perovskite. *Nat. Photon.* 9:695–702
101. Christians JA, Manser JS, Kamat PV. 2015. Multifaceted excited state of $CH_3NH_3PbI_3$. charge separation, recombination, and trapping. *J. Phys. Chem. Lett.* 6:2086–95
102. Beattie AR, Landsberg PT. 1959. Auger effect in semiconductors. *Proc. R. Soc. Lond. A* 249:16–29
103. Nie W, Tsai H, Asadpour R, Blancon JC, Neukirch AJ, et al. 2015. High-efficiency solution-processed perovskite solar cells with millimeter-scale grains. *Science* 347:522–25
104. Shi D, Adinolfi V, Comin R, Yuan M, Alarousu E, et al. 2015. Low trap-state density and long carrier diffusion in organolead trihalide perovskite single crystals. *Science* 347:519–22
105. Zhou H, Chen Q, Li G, Luo S, Song TB, et al. 2015. Interface engineering of highly efficient perovskite solar cells. *Science* 345:542–46
106. Oga H, Saeki A, Ogomi Y, Hayase S, Seki S. 2014. Improved understanding of the electronic and energetic landscapes of perovskite solar cells: high local charge carrier mobility, reduced recombination, and extremely shallow traps. *J. Am. Chem. Soc.* 136:13818–25
107. D'Innocenzo V, Kandada ARS, De Bastiani M, Gandini M, Petrozza A. 2014. Tuning the light emission properties by band gap engineering in hybrid lead halide perovskite. *J. Am. Chem. Soc.* 136:17730–33
108. Edri E, Kirmayer S, Mukhopadhyay S, Gartsman K, Hodes G, Cahen D. 2014. Elucidating the charge carrier separation and working mechanisms of $CH_3NH_3PbI_{3-x}Cl_x$ perovskite solar cells. *Nat. Commun.* 5:3461
109. Wehrenfennig C, Liu M, Snaith HJ, Johnston MB, Herz LM. 2014. Charge carrier recombination channels in the low-temperature phase of organic-inorganic lead halide perovskite thin films. *APL Mater.* 2:081513
110. Guo Z, Manser JS, Wan Y, Kamat PV, Huang L. 2015. Spatial and temporal imaging of long-range charge transport in perovskite thin films by ultrafast microscopy. *Nat. Commun.* 6:7471
111. Sadhanala A, Deschler F, Thomas TH, Dutton SE, Goedel KC, et al. 2014. Preparation of single-phase films of $CH_3NH_3Pb(I_{1-x}Br_x)_3$ with sharp optical band edges. *J. Phys. Chem. Lett.* 5:2501–5
112. Rehman W, Milot RL, Eperon GE, Wehrenfennig C, Boland JL, et al. 2015. Charge-carrier dynamics and mobilities in formamidinium lead mixed-halide perovskites. *Adv. Mater.* 27:7938–44
113. McMeekin DP, Sadoughi G, Rehman W, Eperon GE, et al. 2016. A mixed-cation lead mixed-halide perovskite absorber for tandem solar cells. *Science* 351:151–55
114. Yin WJ, Shi T, Yan Y. 2014. Unusual defect physics in $CH_3NH_3PbI_3$ perovskite solar cell absorber. *Appl. Phys. Lett.* 104:063903

115. Kim J, Lee SH, Lee JH, Hong KH. 2014. The role of intrinsic defects in methylammonium lead iodide perovskite. *J. Phys. Chem. Lett.* 5:1312–17
116. De Wolf S, Holovski J, Moon SJ, Löper P, Niesen B, et al. 2014. Organometal halide perovskites: sharp optical absorption edge and its relation to photovoltaic performance. *J. Phys. Chem. Lett.* 5:1035–39
117. Wu X, Trinh T, Niesner D, Zhu H, Norman Z, et al. 2015. Trap states in lead iodide perovskites. *J. Am. Chem. Soc.* 137:2089–96
118. Samiee M, Konduri S, Ganapathy B, Kottokkaran R, Abbas HA, et al. 2014. Defect density and dielectric constant in perovskite solar cells. *Appl. Phys. Lett.* 105:153502
119. Herz LM, Silva C, Grimsdale AC, Müllen K, Phillips RT. 2004. Time-dependent energy transfer rates in a conjugated polymer guest-host system. *Phys. Rev. B* 70:165207
120. Langevin P. 1903. The recombination and mobilities of ions in gases. *Ann. Chim. Phys.* 28:433–530
121. Yang W, Yao Y, W CQ. 2015. Origin of the high open circuit voltage in planar heterojunction perovskite solar cells: role of the reduced bimolecular recombination. *J. Appl. Phys.* 117:095502
122. Li D, Liang C, Zhang H, Zhang C, You F, He Z. 2015. Spatially separated charge densities of electrons and holes in organic-inorganic halide perovskites. *J. Appl. Phys.* 117:074901
123. Parkinson P, Lloyd-Hughes J, Johnston MB, Herz LM. 2008. Efficient generation of charges via below-gap photoexcitation of polymer-fullerene blend films investigated by terahertz spectroscopy. *Phys. Rev. B* 78:115321
124. de Haas MP, Warman JM, Anthopoulos TD. 2006. The mobility and decay kinetics of charge carriers in pulse-ionized microcrystalline PCBM powder. *Adv. Funct. Mater.* 16:2274–80
125. Pivrikas A, Juška G, Mozer AJ, Scharber M, Arlauskas K, et al. 2005. Bimolecular recombination coefficient as a sensitive testing parameter for low-mobility solar-cell materials. *Phys. Rev. Lett.* 94:176806
126. Adriaenssens GJ, Arkhipov VI. 1997. Non-Langevin recombination in disordered materials with random potential distributions. *Solid State Commun.* 103:541–43
127. Haug A. 1983. Auger recombination in direct-gap semiconductors: band-structure effects. *J. Phys. C* 16:4159–72
128. Haug A. 1988. Band-to-band Auger recombination in semiconductors. *J. Phys. Chem. Solids* 49:599–605
129. Landsberg PT. 1987. The band-band Auger effect in semiconductors. *Solid-State Electron.* 30:1107–15
130. Takeshima M. 1982. Unified theory of the impurity and phonon scattering effects on Auger recombination in semiconductors. *Phys. Rev. B* 25:5390–414

Annual Review of
Physical Chemistry
Volume 67, 2016

Contents

Indexes

Errata

An online log of corrections to *Annual Review of Physical Chemistry* articles may be found at http://www.annualreviews.org/errata/physchem